Dendritic delay lines shape the computation of sound location in neurons of the gerbil medial superior olive

Authors/affiliations

Jared Casarez[1*], Rebecca I. Voglewede[1*], Bradley D. Winters[2], Ken Ledford[1] and Nace L. Golding[1]

* Equal contributions

[1] The University of Texas at Austin, Department of Neuroscience and Center for Learning and Memory, 1 University Station C7000, Austin TX 78712-0248, USA.

[2] Current address: Department of Biological Sciences and University Hospitals – NEOMED Hearing Research Center, Northeast Ohio Medical University, Rootstown, OH, 44272, United States and Brain Health Research Institute, Kent State University, Kent, OH, 44242, United States

Corresponding author and lead contact

Nace L. Golding: The University of Texas at Austin, Department of Neuroscience and Center for Learning and Memory, 1 University Station C7000, Austin TX 78712-0248, golding@austin.utexas.edu.

Summary

In mammals, neurons of the medial superior olive encode information about sounds arising from discrete spatial locations along the horizon. This tuning requires that an internal delay in the brain must offset acoustic disparities to ensure coincident arrival of excitatory inputs driven from the two ears. The source of this optimal internal delay, originally assumed to arise from axonal delay lines, is currently controversial in mammals. Here we use 2-photon guided paired dendritic and somatic recordings together with compartmental modeling of 40 complete MSO neuron morphologies to demonstrate that the dendrites themselves serve as a significant source of internal delay. We show that most MSO neurons exhibit morphological asymmetries that impose different EPSP delays across dendrites and shifts in optimal interaural time differences. Dendrite-based delays in the mammalian MSO are heterogeneous within each isofrequency laminae and provide a stable, structural mechanism to help tune individual neurons to sounds from different azimuthal locations.

Keywords

dendrite; dendritic filtering; coincidence detection; auditory; sound localization.

INTRODUCTION

Spatial information in the auditory system is critical for humans and other mammals to assemble a 3-dimensional view of the world as well as to understand speech and communication signals, especially in environments with many sounds overlapping in time and in frequency. The auditory system is distinct from vision or touch in that there is no explicit peripheral representation of space, in this case in the cochlea, only a representation of frequency. Accordingly, the central auditory system must compute horizontal sound location indirectly by combining a series of monaural and binaural cues [1,2]. Spatial coding in the central auditory system is a prime example of a centrally synthesized or computational map.

Interaural time difference cues are used by birds and mammals to compute horizontal sound location at low frequencies [3]. In mammals this computation takes place in the medial superior olive (MSO), whose neurons are the first to receive converging excitatory and inhibitory inputs driven from the two ears. Intriguingly, in individual neurons, binaural inputs are integrated within a bipolar dendritic architecture, with ipsilateral and contralateral excitatory inputs segregated onto lateral and medial dendritic branches respectively [4,5]. Ipsilateral and contralateral inhibition converges onto the soma and proximal dendrites [4–8]. MSO neurons detect the optimal combination of these inputs, converting temporal coincidence into a rate code [6,9,10].

The concept of internal delay is central to coincidence detection in the MSO, where acoustic delays to the two ears are countered in time by a mechanism of delay inside the brain. This internal temporal asymmetry was postulated in early models to arise from

axonal delay lines formed by ladder-like combinations of bilateral excitatory inputs (the "Jeffress model") [11]. While the Jeffress model enjoys strong support in birds [12–14], comparable studies in mammals have failed to reveal systematic axonal input delay lines nor any mapping of delay along the nucleus [6,15,16]. More recently, there is evidence that fast inhibition mediates internal delay by shifting the peaks of EPSPs [17–19]. However, this mechanism is subject to vigorous debate [20–22], and it is not clear that this mechanism alone can explain the range of receptive field locations in the MSO or their insensitivity to sound level. Other mechanisms have been proposed to mediate internal binaural asymmetry, including asymmetrical axon position, medio-lateral differences in the rising slopes of EPSPs [23], and differences in tuning of binaural inputs ("stereausis") [24,25].

All models of coincidence detection must address the issue of the temporal distortions imposed by the dendrites themselves. However, to date models of MSO neurons have been represented either as point neurons or as simplified, symmetrical "ball-and-stick" models [17,26–30]. Previous measurements of dendritic propagation have revealed that EPSPs encounter delays in their propagation to the soma up to ~150 μs, despite some degree of temporal compensation by activation of low voltage-activated K channels in the soma and proximal dendrites [27]. However, these measurements have largely been restricted to the proximal half of the dendritic arbor and have relied on averaging highly variable populations of neurons. Given that the dendrites of MSO neurons alter their branching pattern and diameters during early hearing and following disruptions of normal hearing [31–33], they might serve as a potential mechanism for adjusting the timing requirements for sounds from the two ears to arrive coincidently at the soma and axon.

Here we demonstrate that the dendritic arbors of MSO neurons are highly heterogeneous and show a striking continuum of asymmetry across the medial and lateral branches that receive segregated inputs driven respectively from the two ears. We show with dual 2-photon fluorescence-guided patch recordings that inputs to smaller and/or more distal dendrites show more substantial propagation delays than previously recognized, and computational modeling of a large population of intact neuronal morphologies shows that these dendritic asymmetries translate into stable internal delays that, as a population, could account for the full range of naturally occurring horizontal locations. Finally, we show that inhibition preserves the effects of dendritic asymmetry on interaural time differences (ITDs) and helps bring the region of maximum slope of firing changes within the ecologically relevant range. Thus dendrite-based delay lines likely work synergistically with other integrative mechanisms purported to shape the perception of horizontal position in mammals.

RESULTS

To understand how MSO neurons process interaural time differences in the dendrites, we made fluorescence-guided dendritic and somatic patch-clamp recordings visualized under 2-photon microscopy. Using this approach, we were able to target the distal third of the dendritic arbor, including secondary and tertiary branches, regions that have largely escaped investigation in these neurons. We then injected simulated EPSCs (τ_{rise} and τ_{decay}, 0.2 ms) into the dendritic pipette and recorded potentials simultaneously at both dendrites and soma. We observed strong variability in both the percent amplitude attenuation at the soma $\left(\left(\frac{V_{soma}}{V_{dend}}\right) \times 100\right)$ as well as the propagation delay of the EPSP,

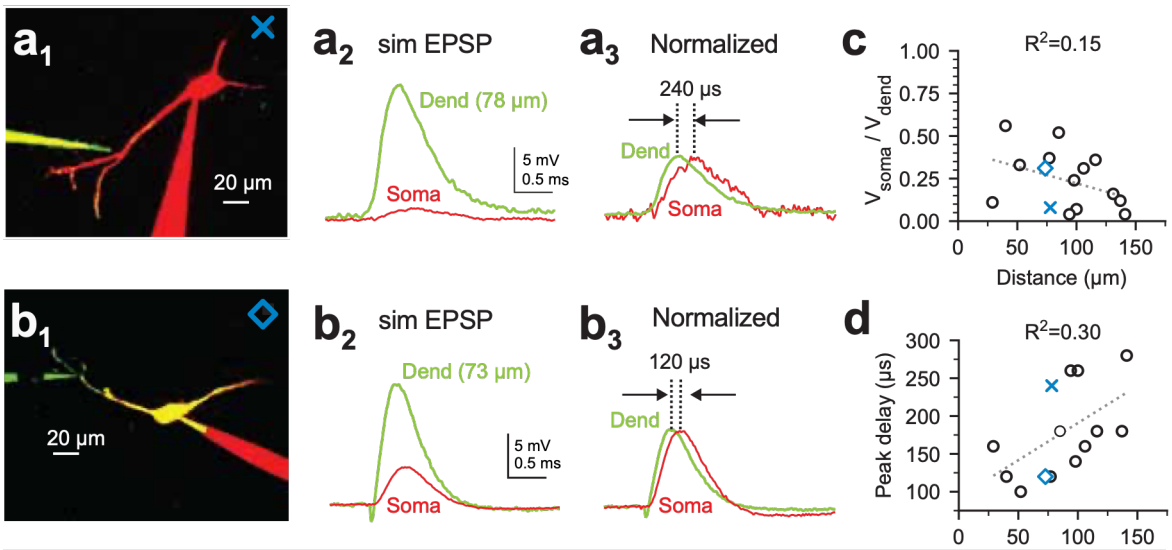

Fig. 1: Heterogeneity in attenuation and timing of simulated excitatory synaptic potentials following propagation from distal dendritic locations to the soma.
a,b, 2-photon fluorescence-guided dual dendritic and somatic patch recordings from two MSO neurons of comparable distances (78 and 73 µm, respectively). Example neuron in **a**$_1$ shows stronger attenuation of somatic propagation of a simulated EPSP (**a**$_2$ vs. **b**$_2$) and longer peak delay (**a**$_3$ vs. **b**$_3$). EPSC amplitudes: cell **a**, 600 pA; cell **b**, 400 pA. **c,d**, Group data for attenuation and peak delay for all paired MSO neuron recordings. There is a poor correlation of both measures as a function of distance.

measured as the difference in EPSP peak time at the soma relative to the dendrite (Fig. 1). Notably, the delays measured in these recordings ranged between 100 and 300 µs, exceeding the physiological range of ITDs measured in gerbils. In these recordings,

there was little correlation between local morphological features of recorded dendrites and propagation delay of the EPSP, measured as the difference in the peak timing of dendritic and somatic EPSPs (Fig. 2a-c). However, there was a stronger correlation between the local dendritic membrane time constant and EPSP propagation delay (Fig. 2d). In addition, there was a weak trend of increasing dendritic membrane time constant

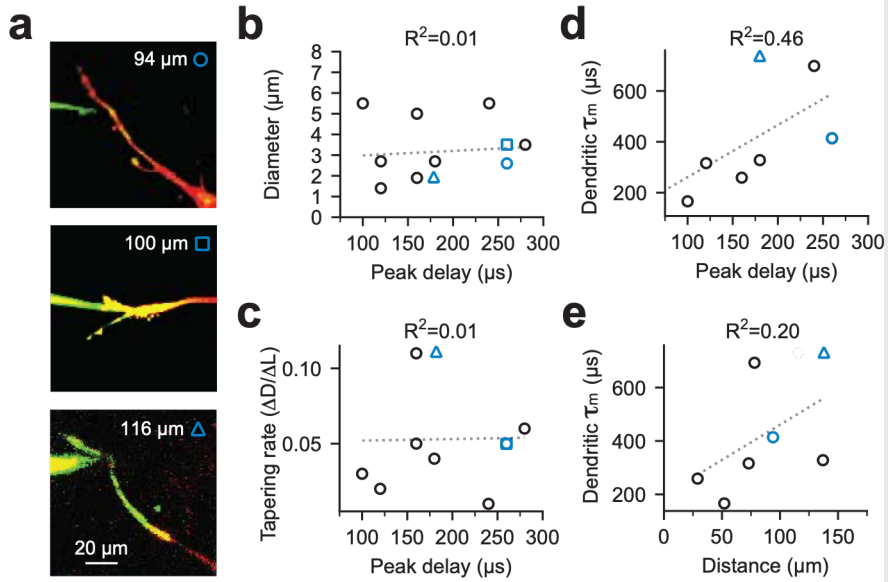

Fig. 2: EPSP propagation delays are not correlated with local morphology but rather more global physiological properties. **a**, Closeups of distal dendritic morphology during paired dendritic and somatic recordings. **b,c**, Delay of peak EPSPs during propagation from dendrite to soma shows no significant correlation with local diameter or tapering rate of local dendrite. (dendritic EPSCs: 400-1000 pA). **d**, Peak EPSP delay from dendrite to soma was weakly correlated with the membrane time constant recorded at the dendritic recording site. **e**, Dendritic membrane time constant increased with distance of the recording site from the soma.

with recording distance (Fig. 2e), possibly because of proximity to the dendritic terminations. These results may reflect that an understanding of the integrative properties of the dendrites requires an analysis of the larger morphological and electrotonic structure of the neuron.

To understand how overall dendritic structure impacts binaural coincidence detection, we analyzed a database of biocytin-filled MSO neurons that exhibited complete dendritic structures (40 of 270 neurons from Bondy et al., 2021 [34] ; Fig. 3). We quantified dendritic length, surface area and branching, with special emphasis on comparisons of medial and lateral dendritic arbors. Higher-order (2° and higher) dendritic branches were prominent in these neurons, comprising 70% of the membrane surface area (Fig. S1).

A striking feature of most neurons in this data set was an overall asymmetry between the lateral and medial dendritic arbors, reflecting differences in length, branching, and/or diameter of the dendrites (Fig. 3a-c). We quantified this asymmetry according to two

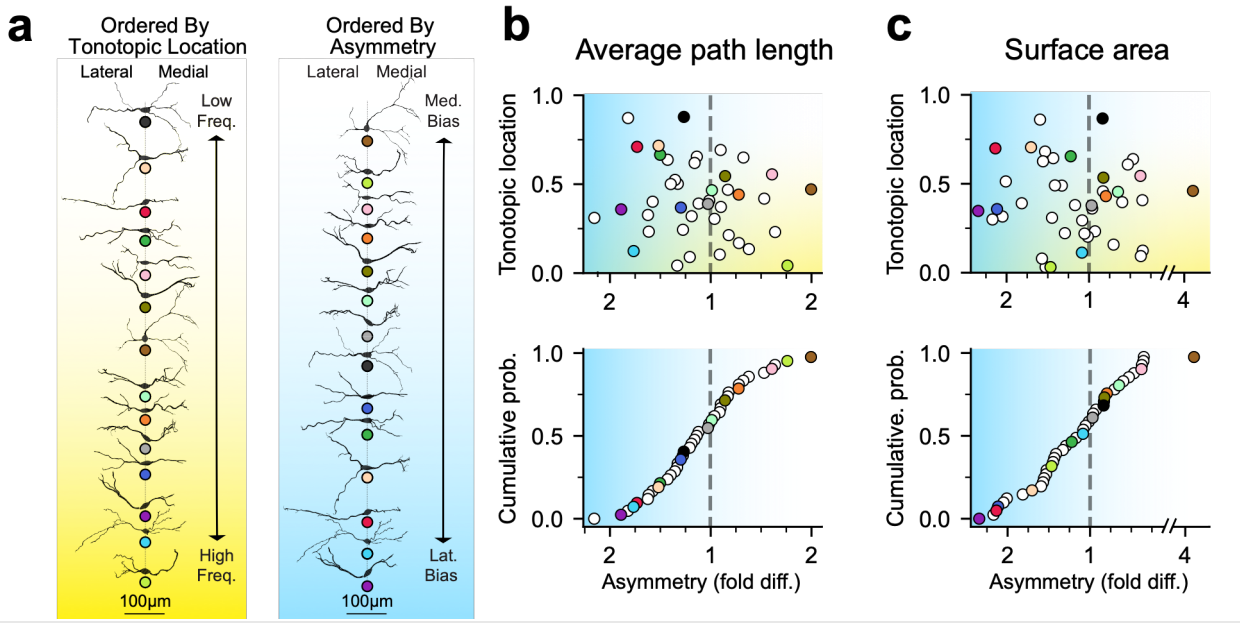

Fig. 3: MSO neuron morphology is inhomogeneous and asymmetric, regardless of tonotopy.
a, Reconstructed morphologies rank ordered by tonotopy (left) and degree of asymmetry (right; average path length). Orderings span from low frequency (top) to high frequency (bottom) and medial (top) and lateral (bottom) asymmetry, respectively. Colored gradients added to visualize ordering. Uniquely colored dots placed beneath each morphology for differentiation. **b**, Fold difference between average path length of medial and lateral dendrites for all reconstructed morphologies (n=40) with vertical axes ordered by tonotopic location (top) or degree of asymmetry (bottom). Gradients added as in **a**. Colored points correspond to **a**. **c**, Same as **b**, except comparing total surface area of medial and lateral branches. Average medio-lateral path length and surface area fold differences (± SEM) were 1.080 ± 0.057 and 1.112 ± 0.133 (biased laterally) and tonotopic R^2 values were -0.42 and -0.23.

parameters, the average path length (average length from each dendritic end to the soma) and membrane surface area, with the latter parameter reflecting the collective influence of dendritic length, diameter and branching pattern. We then defined the degree of bilateral asymmetry as fold differences between the larger vs. smaller dendritic measure for each parameter. We observed no obvious correlation between dendritic asymmetry and tonotopic location (Fig. 3a, *left* and 3b, *top*). However, we found that dendritic asymmetry formed a finely graded continuum, with a slight bias toward lateral dendrites (Fig. 3b, *bottom*). Interestingly, there were no significant differences in population averages of the medio-lateral path length and surface area (1.080 ± 0.057 and

138 1.112 ± 0.133 fold differences; p=0.562), though there was a slight lateral bias. These
139 results indicate that the averaging of dendritic morphological parameters across neurons
140 obscures what is likely a key structural and computational feature.

141 To understand how morphological asymmetry impacts synaptic integration, we
142 constructed compartmental models using the same 40 reconstructions analyzed in Fig. 3.
143 We introduced an excitatory synaptic conductance (alpha function: τ = 290 μs) into each
144 dendritic compartment and then measured the voltage attenuation and propagation delay
145 from the dendritic input location to the soma (Figs. 4-5). At comparable distances from

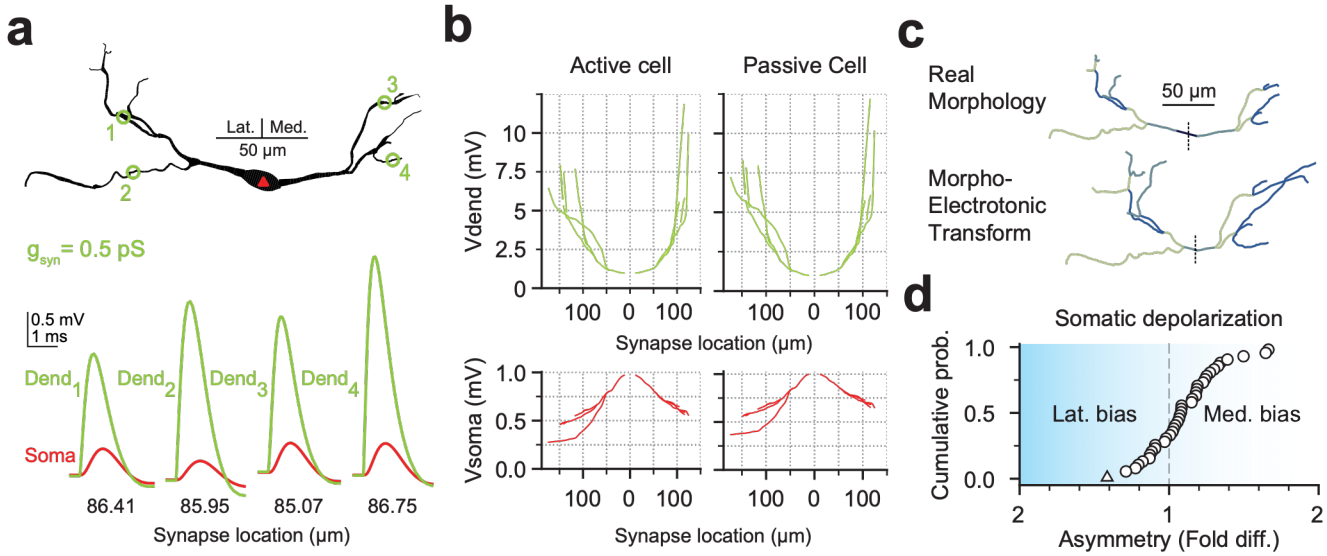

Fig. 4: MSO morphology nonlinearly filters and attenuates propagating EPSPs through its passive cable properties.
a, Visualization EPSP filtering at different dendritic sites. Cell morphology (top) with similarly distant example synaptic sites indicated with green circles and corresponding numbers. Red triangle indicates the somatic compartment. Synaptic conductance indicated as g_{syn}. Four sets of paired dendritic (green) and somatic (red) traces (bottom) for each example synaptic site. Numbering of traces corresponds to labels on morphology above. Dendritic distance from soma for each site indicated below traces. **b**: Same procedure as in **a**, with an adjusted unitary synaptic conductance (see Methods), with measurements from each computational compartment. Model morphology and orientation same as in **a**. Comparison between active channel (left) and passive channel model (right). Recorded EPSP amplitude at synaptic (top, green) and somatic (bottom, red) compartment as a function of distance from soma. **c**, Actual (top) and electrotonically transformed (bottom) morphologies. Transformation visualizes degree of EPSP attenuation from each compartment (see Methods). **d**, Group data (n=40) of average somatic depolarization asymmetry between mediolateral sides. Gradient as in Fig 3. Dotted line indicates equal medial and lateral average somatic depolarizations. Cell from **a-c** indicated with a triangle.

146 the soma, EPSP amplitude at the site of synaptic input and following propagation to the
147 soma varied considerably, like the physiological data from paired recordings in Figure 1

148 (Fig. 4a). Plots of local dendritic and propagated somatic EPSP amplitudes across all
149 synapse locations further revealed striking asymmetries in propagation efficacy of EPSPs
150 to the soma (Fig. 4b, “Active cell”). In MSO neurons, the timing and attenuation of EPSPs
151 along dendrites are influenced both by passive cable filtering as well as interactions with
152 low voltage-activated K channels, which are active in the subthreshold voltage range in
153 these neurons [27] . To determine the degree to which asymmetries in low voltage-activated
154 K channels impact EPSP attenuation at the soma we converted all voltage-activated
155 conductances to leak channels (Fig. 4b, “Passive cell”; see Methods). While EPSPs
156 propagated slightly more effectively to the soma from all dendritic locations in the passive
157 model, it did not fundamentally disrupt mediolateral asymmetry, indicating that these
158 differences arose primarily from the passive electrotonic architecture of the cell. The
159 branching structure had a significant effect on dendritic propagation asymmetry. This
160 could be better visualized in inward morphoelectrotonic transforms of cells, which exhibits
161 dendritic compartments according to their electrotonic, versus physical lengths. In the
162 example neuron in Fig. 4c, large primary dendrites are deemphasized, while thinner
163 secondary and tertiary branches appear as electrotonically elongated. Differences
164 between the medial and lateral dendritic arbors in this neuron and many others gave rise
165 to asymmetries in the magnitude of the average EPSP arriving at the soma.

166 Further, we observed that our population of cells formed a continuum in the degree of
167 somatic depolarization asymmetry, in line with the asymmetry in dendritic structure (Fig.
168 4d). Dendritic asymmetry also translated into differences in average EPSP timing across
169 the medial and lateral dendrites. Figure 5a shows for two example neurons the spatial
170 profile of delays of EPSPs propagating from each dendritic compartment to the soma.

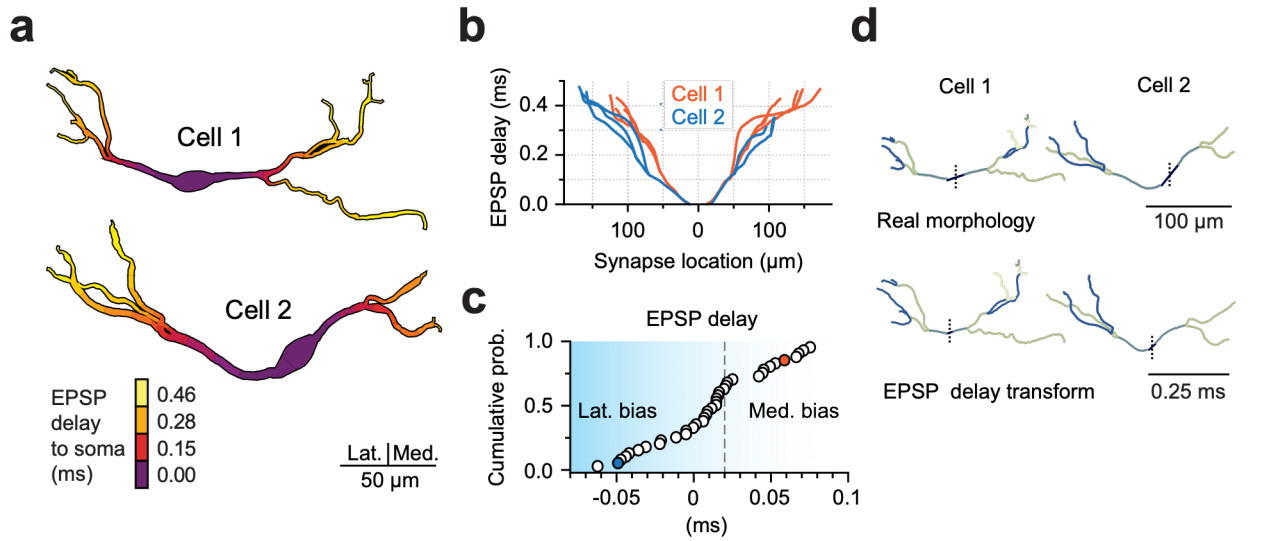

Fig. 5: EPSP timing significantly varies within and between cells, with morphological asymmetry informing overall cell timing. **a,** EPSP delay visualization in two exemplar MSO neurons. Coloring of each cell corresponds to the propagation delay of EPSPs to the soma from its respective compartment. Legend of propagation delay coloring in top right. Cells are oriented mediolaterally according to the scale bar. Outline added to increase gradient readability. **b,** Same data as in **a**, except as a function of distance from the soma. Orientation of cells same as in **a. c**, Group data (n=40) of the difference in average EPSP propagation delay between medial and lateral dendrites. Cells 1 & 2 are indicated with same color as in **b**. Dotted line at 0 ms indicates an equal average EPSP delay between sides. Blue gradient along horizontal axis (as in Fig. 3) to indicate spectrum of asymmetry. **d**, Morphological transforms according to EPSP delays. Morphological centroids of actual cell morphologies (top) and transformed morphologies (bottom). Length corresponds to each sections EPSP delay contribution. Coloring of cell sections is consistent between actual and transformed morphologies for easier differentiation and comparison. Dotted line added to mark the midline.

The asymmetry in dendritic timing can be more quantitatively visualized in plots of peak EPSP delay ($t_{dend} - t_{soma}$) as a function of dendritic distance from the soma (Fig. 5b). Dendritic branch points often introduced substantial jumps in propagation delays, and this is reflected in these plots as increases in slope. To quantify the influence of dendritic asymmetry on the optimal summation of bilateral EPSPs at the soma, we measured the electrotonic delay at the soma for every 2 µm compartment of lateral and medial dendritic subtrees. In our population of 40 neuron models, there were differences in the average relative time of arrival of EPSPs to the soma from compartments in the medial and lateral dendrites. Further, these differences formed a smoothly graded continuum of delays (Fig. 5c).

181 MSO neurons exhibit a range of intrinsic electrical properties, and so we examined a
182 subset of neuron morphologies to understand the functional implications of this
183 physiological diversity. Using a neuron with an asymmetric dendritic arbor, we
184 systematically slowed the membrane time constant by reducing the density of both low
185 voltage-activated K channels and HCN channels (Fig. S2). In both cases, the timing of
186 EPSPs reaching the soma was linearly related to the value of the membrane time
187 constant. Thus, the effects of dendritic asymmetry on EPSP timing and amplitude at the
188 soma are expected to be substantially higher in MSO neurons with slower intrinsic
189 membrane properties. To understand how the differential timing of EPSPs propagating
190 from medial and lateral dendrites is translated into ITDs, we simulated binaural excitatory
191 input using a spiking model of MSO neurons (see Methods). This model featured one
192 axonal input per terminal branch segment as well as a centripetal (dendrite-to-soma)
193 pattern of dendritic innervation, running from the terminal compartments to the soma, in
194 accordance with results from anatomical studies (Fig. 6a) [15,16,28]. The conduction velocity
195 of these inputs was set to 1 ms^{-1}, approximating values of unmyelinated terminal axonal
196 arborizations of similar caliber [13,35] . The timing of ipsilateral and contralateral inputs was
197 varied systematically, triggering spiking only when the two inputs were in close
198 coincidence (Fig. 6b). The location of these excitatory ITD functions were dependent on
199 medio-lateral asymmetry. Functions shifted toward the side of the electrically longer
200 dendrite, reflecting the need for earlier activation of that side to compensate for a longer

201 dendritic propagation delay (Fig. 6c). Our population of 40 neurons showed peak firing at

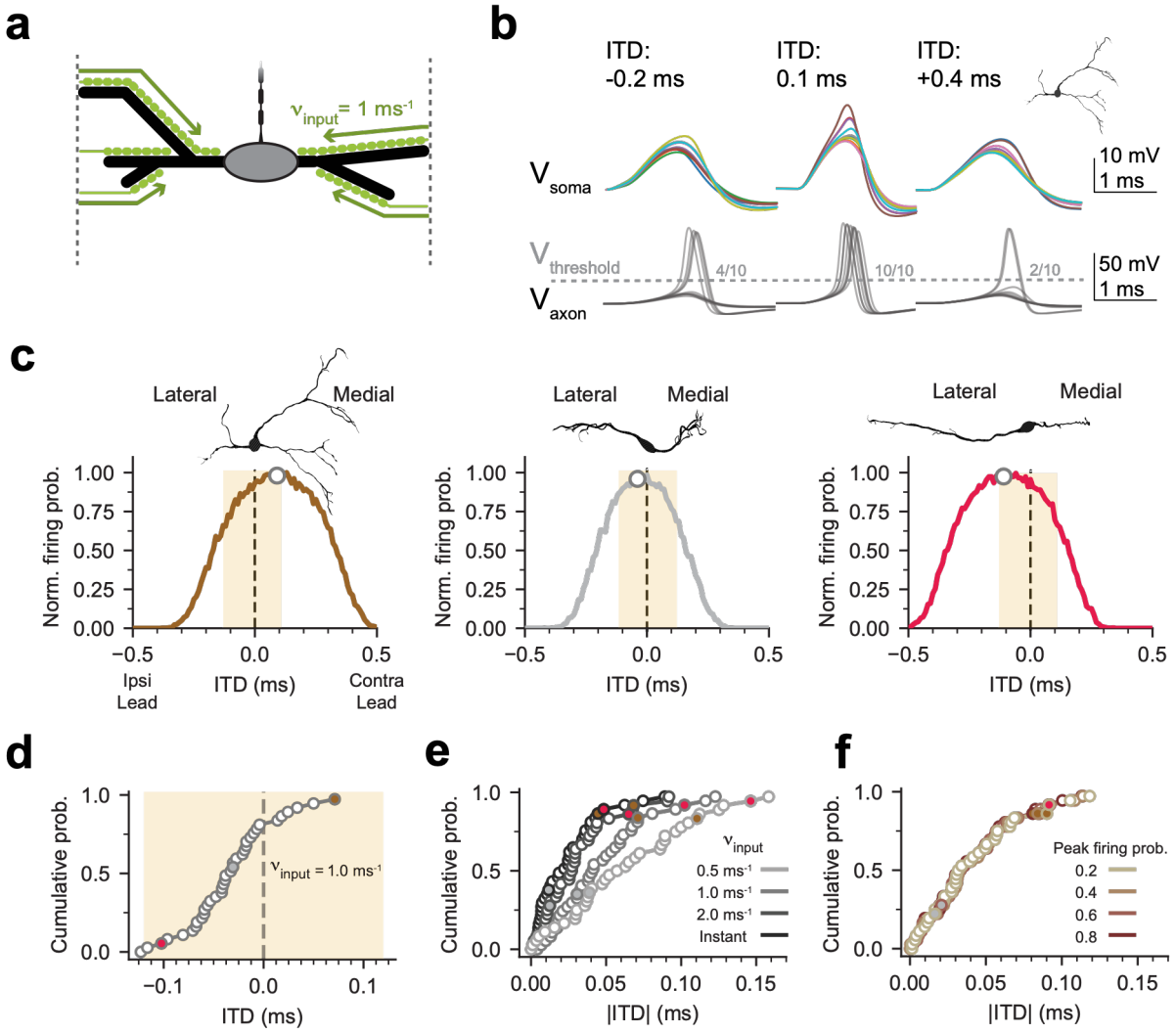

Fig. 6: Simulated ITDs demonstrate conservation of morphological impact on coincident detection. **a**, Schematic visualization of ITD innervation. Somatic compartment and dendrites are shown in gray and black, respectively. Green bulbs represent excitatory synapses, with corresponding arrows to illustrate axonal input velocity (ν_{input}). Dotted lines illustrate point at which there is considered to be no axonal input delay (see Methods). Axon attached to soma, with initial segment, nodes, and internodes. **b**, Example somatic (top) and axonal (bottom) traces from ITD simulations. ITDs of -0.2 ms (left), 0.1 ms (middle, optimal coincidence), 0.3 ms (right) shown. Traces colored only for differentiation. Dotted line ($V_{threshold}$) indicates depolarization threshold for action potential consideration. Morphology of model cell indicated in upper right. **c**, Three example ITD firing curves from varied morphologies, medially biased (left), symmetrical (middle), and laterally biased (right). Corresponding morphologies imaged above. Light orange span represents range of ecologically possible ITDs for model species. Dashed line placed at ITD of 0 ms. Dot indicates centroid ITD value. **d,** Sorted group data (n=39) of centroid ITDs, with ν_{input} = 1 ms^{-1}. Cells from **c** indicated with filled colored points. **e,f**, Sorted group data (n=39) of absolute centroid ITDs, varying axonal input velocity (**e**) and peak firing probability (**f**). Cells from **c** indicated with correspondingly filled colored points.

202 delays that traversed a continuum of values (-0.11 to 0.08 ms, median -0.02; Fig. 6d; Fig.

203 S3). The precise range of values depended in part on the assumptions on the velocity of

204 excitatory axons. The largest range of ITDs was achieved when there was closer
205 matching between the velocity of axonal input velocity and postsynaptic EPSPs
206 propagating from the dendrites to the soma, which maximized temporal coincidence at
207 the soma of spatially disparate inputs in the dendrites (Fig. 6e). Finally, ITDs shifted less
208 than 3% in the face of input amplitude changes that resulted in firing probabilities between
209 0.2 and 0.8, indicating that dendritic asymmetry is highly stable across changing stimulus
210 conditions.

211 Inhibition is a critical component of ITD encoding, although its precise role is subject to
212 vigorous debate. To understand how dendritic asymmetry impacts the effects of inhibition,
213 we added bilateral inhibitory conductances to the somatic compartment of the bilateral
214 excitatory model in Fig. 6, consistent with the known somatically biased innervation of
215 MSO neurons from the lateral and medial nuclei of the trapezoid body (LNTB and
216 MNTB; [8,36]). We set the timing of inhibitory conductances to be 500 μs in advance of
217 excitatory inputs from the same side, in accordance with a previously published
218 estimate [21] . We then adjusted the amplitude of inhibitory conductances to produce
219 summed IPSPs of between ~1-3 mV, which reduced firing probability by 20, 40, 60 and
220 100% (Fig. 7a). With increasing amplitude of IPSPs, resultant ITD functions decreased in
221 halfwidth by 57%, but the location of functions with increasing levels of inhibition were not
222 significantly different from the model with only excitatory inputs (0.070-0.078 ms; centroid,
223 p=0.984; group data). However, the region of maximum slope consistently shifted towards
224 zero, in accordance with a sinking iceberg receptive field scenario (Fig. 7d; -0.27 to 0.07
225 ms). We then tested how the relative timing of excitatory and inhibitory inputs altered ITD
226 functions. Varying the timing of IPSPs relative to EPSPs from –0.5 ms to 0.25 ms altered

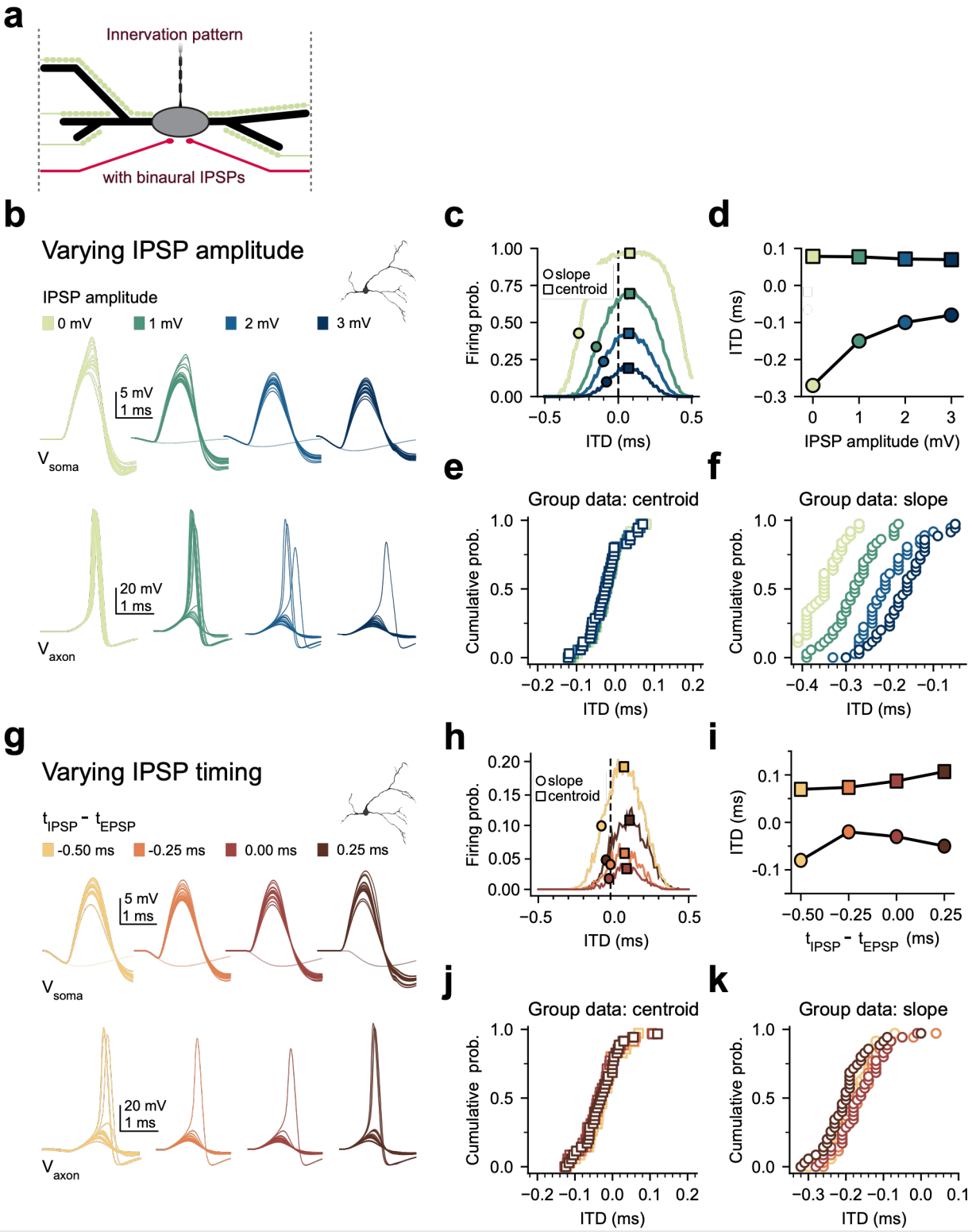

Fig. 7: Inhibition may serve to modulate a pre-established morphological baseline ITD response.
a, Schematic of innervation pattern with excitatory (green) and inhibitory (red) inputs. **b,** Somatic (top) and axonal (bottom) traces from ITD stimulation (ITD: 0.1 ms; IPSP timing: -0.5 ms) for each tested IPSP amplitude. Tested amplitude values and their unique colors above corresponding traces. Morphology of the exemplar neuron shown in the upper right. **c,** Exemplar cell's ITD response curves colored corresponding to IPSP amplitude in **b.** Centroid (square) and maximum slope (circle) are indicated for each curve. Dotted line at an ITD of zero. **d,** ITD centroid and maximum slope as a function of IPSP amplitude (colors corresponding to **b**). **e,f**, Group data (n=39) for ITD centroids (**e**) and steepest sections (**f**) for each IPSP amplitude. Data in **e** are largely overlapping. Shifting of population data in **f** corresponds to trend seen in the exemplar cell (**d**). **g-k**, Same as **b-f**, instead varying the timing of the inhibition (IPSP amplitude: 3 mV). Absolute firing probability, in **h**, is lower than **c**, resulting in lower signal to noise ratio. Centroids in **i** show more variation than **d**, though still minimal. Shift of exemplar cell's maximum slope ITD section (**i**) corresponds to degree of reduction in absolute firing probability (**h**).

228 the location of ITD functions by 0.04 ms, from 0.07 to 0.11 ms. Over the population of
229 MSO neuron morphologies, the presence of inhibition reduced firing probability without
230 fundamentally shifting the location of ITD functions. However, the region of the function
231 where there is maximal change in firing rate is necessarily impacted by the decrease in
232 ITD width (Fig. S4), suggesting that dendritic asymmetry and inhibition provide separate
233 contributions to MSO neurons' receptive field locations.

234

DISCUSSION

The passive cable properties of neuronal dendrites are known to impart both attenuation and delay on EPSPs as they propagate to the soma, commensurate with the distance traversed and the anatomical features of the dendrite itself. However, the functional significance of dendritic geometry and its impact on action potential firing is often difficult to assess. Here we have newly identified a critical function for dendritic structure in the processing of sound localization cues in MSO neurons of the auditory brainstem. We have shown that the bipolar dendritic arbor of MSO neurons is typically asymmetrical, imposing a corresponding asymmetry in the relative timing required for excitatory inputs to drive optimal patterns of action potential output. Our compartmental models show that variation in dendritic morphology across cells exerts a continuum of temporal influences sufficient to shift spatial receptive fields across the full biological range of ITDs available to the gerbil. These shifts are insensitive to differences in intensity and likely work together with other sources of internal delay to enable MSO neurons to stably encode spatial locations along the horizontal plane.

Role of dendritic-based delays in the detection of input sequences

The idea that dendritic structure could dictate detection of temporal sequences of input was first explored in the pioneering computer models of Wilfred Rall. These studies showed that attenuation and propagation delays of EPSPs traveling from the dendrites to the soma could impart greater sensitivity to somatically vs distally directed activation sequences of excitatory inputs, where the longer propagation time of more distal EPSPs is compensated by their earlier activation [37] . Preferential firing to centripetal (distal to

257 proximal) temporal sequences of uncaged glutamate at spines has been demonstrated
258 in cortical neurons in slices, but it is not clear what natural conditions would generate such
259 sequences [38]. By contrast, single excitatory axonal inputs to MSO dendrites mediate a
260 natural centripetal sequence of synaptic activity [15,28,39] , and both current and previous
261 modeling results highlight the importance of matching of input sequence conduction
262 velocity with that of MSO dendrites, which conduct EPSPs at an average of ~0.3 ms^{-1}. In
263 the present study, with the aid of 2-photon fluorescence-guided recordings we have been
264 able to sample smaller diameter secondary and tertiary dendrites at longer distances from
265 the soma. Our results reveal that the attenuation and delays of EPSPs propagating from
266 these processes to the soma are more severe than previously estimated [40] . In our sample
267 of modeled MSO neurons, these slower-conducting non-primary dendrites make up 70%
268 of the surface area of the dendritic arbor in our sample of MSO neurons and thus play an
269 outsized role in exerting temporal shifts in ITD curves in neurons with asymmetrical
270 dendritic trees. These results emphasize that both branching and dendritic diameter are
271 critical determinants of dendritic delay, as seen reflected in the morphoelectrotonic
272 transforms (Fig. 5).

273 In the visual system, asymmetrical length and branching of the dendrites drives temporal
274 disparities in the pattern of inhibition of ganglion cells, providing directional tuning to
275 object movement [41–43]. The computation in the auditory system differs from vision in
276 several fundamental ways. In the retina, spatial information is directly represented at the
277 level of the photoreceptors, and tuning to spatial movement relies on the relative arrival
278 times of excitatory and inhibitory inputs to the dendrites and soma. By contrast, in the
279 cochlea space is not explicitly represented on the basilar membrane, which decomposes

280 complex sounds spatially into different frequency channels. Accordingly, horizontal spatial
281 receptive fields must be constructed *de novo* in the MSO through the detection of synaptic
282 binaural coincidence. In this way, ITDs serve as a proxy for horizontal position.

283 *Other sources of asymmetry in binaural coincidence detection*

284 Although our data reveal that the dendrites may contribute significant interaural delays in
285 the binaural circuitry in the MSO, they likely work together with other mechanisms that
286 have been proposed to influence binaural coincidence detection. In ~25% of MSO
287 neurons in gerbils, the axon emerges from either the lateral or medial dendrites [44,45] , and
288 these results appear to extend to other mammalian species, including guinea pigs and
289 cats [46,47] . Results from computer models suggest these offset axons, like asymmetrical
290 dendrites, introduce strong asymmetries in synaptic integration and ITD tuning [48] .

291 Inhibition has received considerable attention as a mechanism for ITD tuning based on
292 shifts of tuning curves measured in single-unit recordings *in vivo* upon iontophoretic block
293 of glycinergic synapses [18,19] . However, these results are controversial, as strong
294 inhibition has not been observed in both juxtacellular and intracellular patch recordings *in*
295 *vivo* [20,21,49], and there have been concerns about iontophoretic strychnine having off-
296 target effects that that alter both firing probability and input resistance [20]. We found that
297 inhibition did not shift the overall location of ITD curves across the functional range of
298 IPSP magnitudes *(*Fig. 7), consistent with pressure-applied strychnine data *in vivo* [20].
299 Inhibition shifted the location of maximal change in firing rate, consistent with a
300 conventional "iceberg" model of inhibitory action on neuronal receptive fields. In
301 mammals, the maximum rate of change, or slope of ITDs may be more important for

302 population encoding of ITDs. Given that the maximal rising slope of firing invariably shifts
303 toward 0 μs ITD when inhibition narrows ITD curves, both inhibition and dendritic
304 asymmetry would both play key roles in setting the location of individual MSO neurons'
305 receptive fields.

306 *Comparison with avian binaural coincidence detectors.*

307 Binaural coincidence detection has been extensively studied in birds, and thus the
308 comparison to mammals is noteworthy. Unlike mammals, dendritic morphology in bird
309 MSO (nucleus laminaris) shows striking dependence on tonotopic location, exhibiting
310 longer, more highly branched dendrites in neurons from low frequency regions [33,50]. While
311 these tonotopic differences in dendritic length have garnered considerable attention, a
312 close examination of dendritic parameters shows that nucleus laminaris neurons, like
313 those in mammalian MSO, exhibit a continuum of dendritic asymmetry in the length of
314 dendrites receiving ipsilateral and contralateral inputs (Smith and Rubel 1979, their Fig.
315 15 [33]). In these low frequency regions, inputs are restricted to distal, higher order
316 branches [51]. Based on both our electrophysiological and modeling data, these higher
317 order branches incur the largest delays as compared to the large-caliber primary
318 dendrites and thus would be the primary determinants of dendritic propagation delay on
319 each side. In the more highly specialized barn owls, the dendrites of laminaris neurons
320 are more limited, and thus internal delay compensation must lie squarely on those
321 provided by unmyelinated afferents [13] .

322 *Dendritic morphology and the scaling problem across species.*

323 The biological range of ITDs varies with head size [52,53], and thus any mechanism of
324 internal delay must be scalable across species, accounting for ITDs differing by hundreds
325 of microseconds (e.g., gerbil: ±130 μs [54], human: ± 600-700 μs [55]). A dendrite-based
326 source of internal delay would be easily scalable, as the length of MSO dendrites
327 increases with the size of different species. Although quantitative data are not available,
328 previous morphological studies in guinea pig, ferret, cat and humans show that the
329 dendritic arbors show considerable asymmetries [46,47,56,57].

330

331 **METHODS**

332 All procedures were conducted in agreement with the Institutional Animal Care and Use
333 Committee at The University of Texas at Austin (UT-Austin), which followed the guidelines
334 of the National Institutes of Health. Mongolian gerbils (*Meriones unguiculatus*) were
335 housed and raised in a colony at the UT-Austin Animal Resource Center. Animals
336 experienced a 50/50 day/night cycle and had continuous access to food and water.

337 *Brain slice preparation*: both male and female gerbils (17-40 days old) were anesthetized
338 with isoflurane and decapitated upon loss of the choroid reflex. The brain was removed
339 from the cranium under warm (34-35°C) artificial cerebrospinal fluid (ACSF), the
340 cerebellum was removed and the isolated hindbrain was glued to the stage of an
341 oscillating tissue slicer (Leica VT-1200S). Horizontal sections were prepared at 200 μm
342 thickness and stored at 35°C in a holding chamber for 45-60 min., and then gradually
343 cooled to room temperature (24°C). All solutions were continuously bubbled with
344 95% O_2 / 5% CO_2. ACSF contained (in mM): 125 mM NaCl, 25 mM D-glucose, 2.5 mM

345 KCl, 25 mM $NaHCO_3$, 1.25 mM NaH_2PO_4, 1.5mM $MgSO_4$, 1.5 mM $CaCl_2$, pH adjusted to
346 7.45 with NaOH, and final osmolarity at 315 mOsm.

347 *Imaging and electrophysiological acquisition and analyses:* neurons in the MSO were
348 visualized under gradient contrast optics on a Leica TCS SP5 System equipped with a
349 Coherent Chameleon Ultra II Ti:sapphire laser and an 8 kHz resonant scanner under
350 control of Leica LAS AF Imaging Software. We found that gradient contrast images
351 acquired via the photomultiplier tubes were of poor contrast in the heavily myelinated
352 regions of the auditory brainstem, and so cell selection and seal formation was carried
353 out under gradient contrast imaging through the epifluorescence port of the microscope
354 and detected on a high-resolution monochrome digital camera (Zeiss Axiocam 503)
355 running Zen software. The soma was recorded in whole-cell current clamp mode with a
356 pipette (4 to 8 MΩ resistance) containing a potassium gluconate-based solution with 40-
357 80 μM Alexa 594 added for visualizing cell morphology. After waiting ~10 min. for the dye
358 to fill the dendritic arbor, a dendritic recording was made under 2-photon fluorescence
359 with a second pipette (8 to 15 MΩ resistance) containing the same K Gluconate solution
360 with 40-80 μM Alexa 488. Pipette solutions had a composition of 115 mM K-gluconate,
361 4.42 mM KCl, 0.5 mM EGTA, 10 mM HEPES, 10 mM, Na_2Phosphocreatine, 4 mM MgATP,
362 and 0.3 mM NaGTP. Osmolality was adjusted to 300 mOsm/L with sucrose, and pH was
363 adjusted to 7.30 with KOH. Seal resistances exceeded 1 GΩ, and recordings were
364 discontinued if series resistances exceeded 20 or 50 MΩ for somatic and dendritic
365 recordings, respectively.
366 Electrophysiological recordings were under the control of custom routines written in
367 IGOR-Pro (Wavemetrics). Pipettes were prepared on a Sutter P-1000 puller using

368 borosilicate glass (1.5 mm O.D.). Data was acquired using a pair of Dagan BVC-700,
369 amplifiers in conjunction with an ITC-18 computer interface (Heka Instruments). Data was
370 low-pass filtered at 5 kHz, sampled at 50 kHz, and stored on a Macintosh computer for
371 further analyses using custom-written routines in IGOR-Pro.

372 *Compartment model construction:*

373 A subpopulation of 40 fully intact reconstructed MSO neurons was selected from those
374 gathered in Bondy et al. (2021) [34] . The reconstructed morphologies were imported into
375 the NEURON simulation environment, using its Neurolucida importing tool.
376 Computational compartments were created every 2 μm (Fig. S5a). Somatic and dendritic
377 compartments were applied channel kinetics differentially, consisting of low and high-
378 voltage-activated K channels [27,58] , HCN channels[59] , and leak channels, with sodium
379 channels[60] exclusively in the somatic compartments. In simulations modeling a passive
380 cell, high and low-voltage potassium and HCN channels were replaced with passive leak
381 channels with conductances set to the average resting conductance of the preexisting
382 active channels. In simulations with an axon, a model axon, with morphology as in
383 Lehnert (2014) [61] , was attached at the center of the model soma. The axon channel
384 kinetics implemented consisted of sodium channels, low-threshold potassium channels
385 and leak channels in the nodes and initial segments, with solely leak channels in the
386 internodes. Measurements from the axon were all recorded from the fifth node. Simulated
387 synapses were conductance-based and shaped by an alpha function (τ = 290 μs).

388

Channel	Dendrite	Soma	TAIS	CAIS	Internode	Node
KLT (Mathews, 2010)	20	40	155	155		155
KHT (Nabel, 2019)	0.55	0.55				
HCN (Khurana, 2011)	1	1	2	2		
Na (Scott, 2010)	0	30	250	250		250
Leak	0.05	0.05	0.05	0.05	0.02	5

Table 1: Maximal channel conductances (μS/cm^2). Tapered axon initial segment (TAIS) and constant disameter axon initial segment (CAIS).

389 *Simulation variations:* When measuring EPSP propagation, synapses were placed every
390 2 μm, with a unitary conductance that would maximally depolarize the soma 1 mV (unless
391 noted otherwise). Each synapse was then stimulated and recorded separately. In ITD
392 coincident detection procedures, dendrites were innervated with synapses (release
393 probability=0.45) placed every 2 μm, totaling ~125 synapses for each side [62] . To mimic
394 axonal activation, an artificial axonal input delay (Δt_{axon}) was calculated for each synapse
395 as a function of conduction velocity (ν_{input}) and axonal travel distance. The travel distance
396 was considered zero at each side's furthest point from the soma. Otherwise, the axonal
397 travel distance consists of two components: the mediolateral distance from the furthest
398 point (Δt_{axon}=0) to the synapse's closest terminal segment; the path length from that
399 terminal segment to the synapse (Fig. S5b). Artificial ITDs could then be added onto the
400 calculated axonal delay. Each artificial ITD value (-0.5 to 0.5 ms, incremented by 0.01),
401 was tested with 400 trials, and each trial consisted of a single stimulation of all synapses.
402 To provide a more binary output, a model axon was attached to the cell's soma, and a
403 spike was reported if a 25 mV depolarization from rest was recorded at the fifth and final

404 axonal node. The synapses could then be adjusted with a unitary conductance to achieve
405 an acceptable maximum firing probability. When implementing IPSP inputs to the ITD
406 procedure, two inhibitory synapses were added at the soma, one corresponding to each
407 mediolateral side. Each synapse generated an IPSP shaped by an alpha function with a
408 time constant of 1.5 ms [62]. The timing of the synapses was adjusted relative to the
409 artificial excitatory ITD signals. The amplitude of the IPSPs was adjusted by modifying
410 the inhibitory synapses' conductances to achieve a combined IPSP hyperpolarization of
411 approximately 1, 2, and 3 mV.

412 *Data analyses*

413 Measures of dendritic distance, both in slice experiments and in compartment models,
414 were taken as the length along the dendritic arbor to the center of the somatic
415 compartment. To address the variable size of the MSO within the slice plane, a normalized
416 tonotopic location was calculated as the cell's distance from the most dorsal point of the
417 MSO, relative to the entire MSO dorsoventral length. To provide a quantitative value of
418 asymmetry between each cell's morphological measures, a unit of fold difference
419 $\left(\log_2\left(\frac{\max\{\text{medial},\ \text{lateral}\}}{\min\{\text{medial},\ \text{lateral}\}}\right)+1\right)$ was used, with a value of 1 and 2 representing equal and
420 double values, respectively. Average path length measurements were taken from the
421 distances along the dendrite to the soma from each terminal section of the corresponding
422 mediolateral arbor. Measurements for propagation attenuation and timing were taken at
423 both the synaptic and somatic compartments of the model cell. For attenuation, the
424 somatic depolarization for mediolateral sides was calculated by averaging each synaptic
425 compartments propagated EPSP amplitude at the soma. Morpho-electrotonic transforms

were created by scaling each sections length according to the natural logarithm of its attenuation $\left(\text{section length} = \ln\left(\frac{V_{dend}}{V_{soma}}\right)\right)$. EPSP delay values were calculated by measuring the time between peak depolarization in the synaptic and somatic compartments. The corresponding delay transforms are scaled according to the delay contribution of each section. Mediolateral comparisons of delay were calculated by subtracting each sides average EPSP delay for all compartments. To minimize noise and data filtering for the ITD response, the centroid of the curve was measured, where half of the total area under the curve exists on either side. Comparisons were made using the absolute ITD centroid values to highlight the population of neurons' collective change. The ITD firing probabilities were smoothed with a Savitzky–Golay filter for the purpose of reasonably identifying the region of max slope for the curves.

438 **REFERENCES**

439

440 1. Grothe, B., and Pecka, M. (2014). The natural history of sound localization in
441 mammals--a story of neuronal inhibition. Front Neural Circuits *8*, 116.
442 https://doi.org/10.3389/fncir.2014.00116.

443 2. Joris, P., and Yin, T.C. (2007). A matter of time: internal delays in binaural
444 processing. Trends Neurosci *30*, 70–78. https://doi.org/10.1016/j.tins.2006.12.004.

445 3. Carr, C.E., Soares, D., Parameshwaran, S., and Perney, T. (2001). Evolution and
446 development of time coding systems. Current Opinion in Neurobiology *11*, 727–733.
447 https://doi.org/10.1016/s0959-4388(01)00276-8.

448 4. Stotler, W.A. (1953). An experimental study of the cells and connections of the
449 superior olivary complex of the cat. J Comp Neurol *98*, 401–431.

450 5. Lindsey, B.G. (1975). Fine structure and distribution of axon terminals from the
451 cochlear nucleus on neurons in the medial superior olivary nucleus of the cat. J Comp
452 Neurol *160*, 81–103. https://doi.org/10.1002/cne.901600106.

453 6. Yin, T.C., and Chan, J.C. (1990). Interaural time sensitivity in medial superior olive of
454 cat. J Neurophysiol *64*, 465–488.

455 7. Magnusson, A.K., Kapfer, C., Grothe, B., and Koch, U. (2005). Maturation of
456 glycinergic inhibition in the gerbil medial superior olive after hearing onset. J Physiol
457 *568*, 497–512. https://doi.org/10.1113/jphysiol.2005.094763.

458 8. Kapfer, C., Seidl, A.H., Schweizer, H., and Grothe, B. (2002). Experience-dependent
459 refinement of inhibitory inputs to auditory coincidence-detector neurons. Nat Neurosci *5*,
460 247–253. https://doi.org/10.1038/nn810.

461 9. Spitzer, M.W., and Semple, M.N. (1995). Neurons sensitive to interaural phase
462 disparity in gerbil superior olive: diverse monaural and temporal response properties. J
463 Neurophysiol *73*, 1668–1690.

464 10. Goldberg, J.M., and Brown, P.B. (1969). Response of binaural neurons of dog
465 superior olivary complex to dichotic tonal stimuli: some physiological mechanisms of
466 sound localization. J Neurophysiol *32*, 613–636.

467 11. Jeffress, L.A. (1948). A place theory of sound localization. J Comp Physiol Psychol
468 *41*, 35–39.

469 12. Carr, C.E., and Konishi, M. (1988). Axonal delay lines for time measurement in the
470 owl's brainstem. Proc Natl Acad Sci U S A *85*, 8311–8315.

471 13. Carr, C., and Konishi, M. (1990). A circuit for detection of interaural time differences
472 in the brain stem of the barn owl.

473 14. Moiseff, A., and Konishi, M. (1981). Neuronal and behavioral sensitivity to binaural
474 time differences in the owl. J Neurosci *1*, 40–48. https://doi.org/10.1523/jneurosci.01-01-
475 00040.1981.

476 15. Beckius, G.E., Batra, R., and Oliver, D.L. (1999). Axons from anteroventral cochlear
477 nucleus that terminate in medial superior olive of cat: observations related to delay
478 lines. J Neurosci *19*, 3146–3161.

479 16. Smith, P.H., Joris, P.X., Carney, L.H., and Yin, T.C. (1991). Projections of
480 physiologically characterized globular bushy cell axons from the cochlear nucleus of the
481 cat. J Comp Neurol *304*, 387–407. https://doi.org/10.1002/cne.903040305.

482 17. Myoga, M.H., Lehnert, S., Leibold, C., Felmy, F., and Grothe, B. (2014). Glycinergic
483 inhibition tunes coincidence detection in the auditory brainstem. Nat Commun *5*, 3790.
484 https://doi.org/10.1038/ncomms4790.

485 18. Pecka, M., Brand, A., Behrend, O., and Grothe, B. (2008). Interaural time difference
486 processing in the mammalian medial superior olive: the role of glycinergic inhibition. J
487 Neurosci *28*, 6914–6925. https://doi.org/10.1523/jneurosci.1660-08.2008.

488 19. Brand, A., Behrend, O., Marquardt, T., McAlpine, D., and Grothe, B. (2002). Precise
489 inhibition is essential for microsecond interaural time difference coding. Nature *417*,
490 543–547. https://doi.org/10.1038/417543a.

491 20. Franken, T.P., Roberts, M.T., Wei, L., Golding, N.L., and Joris, P.X. (2015). In vivo
492 coincidence detection in mammalian sound localization generates phase delays. Nat
493 Neurosci *18*, 444–452. https://doi.org/10.1038/nn.3948.

494 21. Roberts, M.T., Seeman, S.C., and Golding, N.L. (2013). A mechanistic
495 understanding of the role of feedforward inhibition in the mammalian sound localization
496 circuitry. Neuron *78*, 923–935. https://doi.org/10.1016/j.neuron.2013.04.022.

497 22. Heijden, M. van der, Lorteije, J.A., Plauska, A., Roberts, M.T., Golding, N.L., and
498 Borst, J.G. (2013). Directional hearing by linear summation of binaural inputs at the
499 medial superior olive. Neuron *78*, 936–948.
500 https://doi.org/10.1016/j.neuron.2013.04.028.

501 23. Jercog, P.E., Svirskis, G., Kotak, V.C., Sanes, D.H., and Rinzel, J. (2010).
502 Asymmetric excitatory synaptic dynamics underlie interaural time difference processing
503 in the auditory system. PLoS Biol *8*, e1000406.
504 https://doi.org/10.1371/journal.pbio.1000406.

24. Shamma, S.A., Shen, N., and Gopalaswamy, P. (1989). Stereausis: binaural processing without neural delays. The Journal of the Acoustical Society of America *86*, 989–1006. https://doi.org/10.1121/1.398734.

25. Plauška, A., Heijden, M.V.D., and Borst, J.G.G. (2017). A test of the stereausis hypothesis for sound localization in mammals. Journal of Neuroscience *37*, 7278–7289. https://doi.org/10.1523/jneurosci.0233-17.2017.

26. Agmon-Snir, H., Carr, C.E., and Rinzel, J. (1998). The role of dendrites in auditory coincidence detection. Nature *393*, 268–272. https://doi.org/10.1038/30505.

27. Mathews, P.J., Jercog, P.E., Rinzel, J., Scott, L.L., and Golding, N.L. (2010). Control of submillisecond synaptic timing in binaural coincidence detectors by K(v)1 channels. Nat Neurosci *13*, 601–609. https://doi.org/10.1038/nn.2530.

28. Callan, A.R., Hess, M., Felmy, F., and Leibold, C. (2021). Arrangement of Excitatory Synaptic Inputs on Dendrites of the Medial Superior Olive. J Neurosci *41*, 269–283. https://doi.org/10.1523/jneurosci.1055-20.2020.

29. Franken, T.P., Bremen, P., and Joris, P.X. (2014). Coincidence detection in the medial superior olive: Mechanistic implications of an analysis of input spiking patterns. Frontiers in Neural Circuits *8*, 42. https://doi.org/10.3389/fncir.2014.00042.

30. Dasika, V.K., White, J.A., and Colburn, H.S. (2007). Simple models show the general advantages of dendrites in coincidence detection. J Neurophysiol *97*, 3449–3459. https://doi.org/10.1152/jn.00669.2005.

31. Feng, A.S., and Rogowski, B.A. (1980). Effects of monaural and binaural occlusion on the morphology of neurons in the medial superior olivary nucleus of the rat. Brain Research *189*, 530–534. https://doi.org/10.1016/0006-8993(80)90112-2.

32. Russell, F.A., and Moore, D.R. (1999). Effects of unilateral cochlear removal on dendrites in the gerbil medial superior olivary nucleus. Eur J Neurosci *11*, 1379–1390.

33. Smith, D.J., and Rubel, E.W. (1979). Organization and development of brain stem auditory nuclei of the chicken: dendritic gradients in nucleus laminaris. J Comp Neurol *186*, 213–239. https://doi.org/10.1002/cne.901860207.

34. Bondy, B.J., Haimes, D.B., and Golding, N.L. (2021). Physiological diversity influences detection of stimulus envelope and fine structure in neurons of the medial superior olive. J Neurosci. https://doi.org/10.1523/jneurosci.2354-20.2021.

35. Hoffmeister, B., Jänig, W., and Lisney, S.J.W. (1991). A proposed relationship between circumference and conduction velocity of unmyelinated axons from normal and regenerated cat hindlimb cutaneous nerves. Neuroscience *42*, 603–611. https://doi.org/10.1016/0306-4522(91)90402-a.

36. Werthat, F., Alexandrova, O., Grothe, B., and Koch, U. (2008). Experience-dependent refinement of the inhibitory axons projecting to the medial superior olive. Dev Neurobiol *68*, 1454–1462. https://doi.org/10.1002/dneu.20660.

37. Rinzel, J., and Rall, W. (1974). Transient response in a dendritic neuron model for current injected at one branch. Biophys J *14*, 759–790. https://doi.org/10.1016/s0006-3495(74)85948-5.

38. Branco, T., Clark, B.A., and Häusser, M. (2010). Dendritic discrimination of temporal input sequences in cortical neurons. Science *329*, 1671–1675. https://doi.org/10.1126/science.1189664.

39. Smith, P.H., Joris, P.X., and Yin, T.C. (1993). Projections of physiologically characterized spherical bushy cell axons from the cochlear nucleus of the cat: evidence for delay lines to the medial superior olive. J Comp Neurol *331*, 245–260. https://doi.org/10.1002/cne.903310208.

40. Winters, B.D., Jin, S.X., Ledford, K.R., and Golding, N.L. (2017). Amplitude Normalization of Dendritic EPSPs at the Soma of Binaural Coincidence Detector Neurons of the Medial Superior Olive. J Neurosci *37*, 3138–3149. https://doi.org/10.1523/jneurosci.3110-16.2017.

41. Bloomfield, S.A. (1994). Orientation-sensitive amacrine and ganglion cells in the rabbit retina. Journal of Neurophysiology *71*, 1672–1691. https://doi.org/10.1152/jn.1994.71.5.1672.

42. Trenholm, S., Johnson, K., Li, X., Smith, R.G., and Awatramani, G.B. (2011). Parallel mechanisms encode direction in the retina. Neuron *71*, 683–694. https://doi.org/10.1016/j.neuron.2011.06.020.

43. Bloomfield, S.A. (1991). Two types of orientation-sensitive responses of amacrine cells in the mammalian retina. Nature *350*, 347–350. https://doi.org/10.1038/350347a0.

44. Scott, L.L., Mathews, P.J., and Golding, N.L. (2005). Posthearing developmental refinement of temporal processing in principal neurons of the medial superior olive. J Neurosci *25*, 7887–7895. https://doi.org/10.1523/jneurosci.1016-05.2005.

45. Rautenberg, P.L., Grothe, B., and Felmy, F. (2009). Quantification of the three-dimensional morphology of coincidence detector neurons in the medial superior olive of gerbils during late postnatal development. J Comp Neurol *517*, 385–396. https://doi.org/10.1002/cne.22166.

46. Cajal., S.R.Y. (1907). Structure et connexions des neurones. Nordiskt Medicinskt Arkiv *40*, 1–28. https://doi.org/10.1111/j.0954-6820.1907.tb00034.x.

47. Smith, P.H. (1995). Structural and functional differences distinguish principal from nonprincipal cells in the guinea pig MSO slice. J. Neurophysiol. *73*, 1653–1667. https://doi.org/10.1152/jn.1995.73.4.1653.

48. Zhou, Y., Carney, L.H., and Colburn, H.S. (2005). A model for interaural time difference sensitivity in the medial superior olive: interaction of excitatory and inhibitory synaptic inputs, channel dynamics, and cellular morphology. J Neurosci *25*, 3046–3058. https://doi.org/10.1523/jneurosci.3064-04.2005.

49. Plauska, A., Borst, J.G., and Heijden, M. van der (2016). Predicting binaural responses from monaural responses in the gerbil medial superior olive. J Neurophysiol *115*, jn 01146 2015. https://doi.org/10.1152/jn.01146.2015.

50. Wang, Y., and Rubel, E.W. (2008). Rapid regulation of microtubule-associated protein 2 in dendrites of nucleus laminaris of the chick following deprivation of afferent activity. Neuroscience *154*, 381–389. https://doi.org/10.1016/j.neuroscience.2008.02.032.

51. Yamada, R., and Kuba, H. (2021). Dendritic synapse geometry optimizes binaural computation in a sound localization circuit. Science Advances *7*. https://doi.org/10.1126/sciadv.abh0024.

52. Jones, H.G., Koka, K., Thornton, J.L., and Tollin, D.J. (2011). Concurrent development of the head and pinnae and the acoustical cues to sound location in a precocious species, the chinchilla (Chinchilla lanigera). J Assoc Res Otolaryngol *12*, 127–140. https://doi.org/10.1007/s10162-010-0242-3.

53. Koka, K., Jones, H.G., Thornton, J.L., Lupo, J.E., and Tollin, D.J. (2011). Sound pressure transformations by the head and pinnae of the adult Chinchilla (Chinchilla lanigera). Hear Res *272*, 135–147. https://doi.org/10.1016/j.heares.2010.10.007.

54. Maier, J.K., and Klump, G.M. (2006). Resolution in azimuth sound localization in the Mongolian gerbil (Meriones unguiculatus) . The Journal of the Acoustical Society of America *119*, 1029–1036. https://doi.org/10.1121/1.2159429.

55. George, K. (1977). Model for the intramural time differences in the azimuthal plane. J. Acoust. Soc. Am *62*, 157–167.

56. Henkel, C.K., and Brunso-Bechtold, J.K. (1990). Dendritic morphology and development in the ferret medial superior olivary nucleus. J Comp Neurol *294*, 377–388. https://doi.org/10.1002/cne.902940307.

57. Kulesza, R. (2008). Cytoarchitecture of the human superior olivary complex: nuclei of the trapezoid body and posterior tier. Hear Res *241*, 52–63. https://doi.org/10.1016/j.heares.2008.04.010.

58. Nabel, A.L., Callan, A.R., Gleiss, S.A., Kladisios, N., Leibold, C., and Felmy, F. (2019). Distinct distribution patterns of potassium channel sub-units in somato-dendritic compartments of neurons of the medial superior olive. Frontiers in Cellular Neuroscience *13*, 409471. https://doi.org/10.3389/fncel.2019.00038/bibtex.

59. Khurana, S., Liu, Z., Lewis, A.S., Rosa, K., Chetkovich, D., and Golding, N.L. (2012). An essential role for modulation of hyperpolarization-activated current in the development of binaural temporal precision. J Neurosci *32*, 2814–2823. https://doi.org/10.1523/jneurosci.3882-11.2012.

60. Scott, L.L., Mathews, P.J., and Golding, N.L. (2010). Perisomatic voltage-gated sodium channels actively maintain linear synaptic integration in principal neurons of the medial superior olive. J Neurosci *30*, 2039–2050. https://doi.org/10.1523/jneurosci.2385-09.2010.

61. Lehnert, S., Ford, M.C., Alexandrova, O., Hellmundt, F., Felmy, F., Grothe, B., and Leibold, C. (2014). Action potential generation in an anatomically constrained model of medial superior olive axons. J Neurosci *34*, 5370–5384. https://doi.org/10.1523/jneurosci.4038-13.2014.

62. Couchman, K., Grothe, B., and Felmy, F. (2010). Medial superior olivary neurons receive surprisingly few excitatory and inhibitory inputs with balanced strength and short-term dynamics. J Neurosci *30*, 17111–17121. https://doi.org/10.1523/jneurosci.1760-10.2010.